Waste and Biomass Valorization
https://doi.org/10.1007/s12649-021-01585-w

ORIGINAL PAPER

Petcoke Revalorization as Support for ZnO-based Photocatalyst

J. A. Arcibar-Orozco[1] · H. E. Zili-Tomita[1] · V. A. Suárez-Toriello[2] · J. O. Saucedo-Lucero[1]

Received: 8 March 2021 / Accepted: 14 September 2021

Abstract

Petcoke is a residue from the petroleum oil industry which, due to its physicochemical characteristics and content of organic and inorganic material, can be exploited and revalued in order to be used to improve the photocatalytic properties of different semiconductors. With this in mind, the present work shows the evaluation of petcoke as a support material to ZnO to reduce organic pollutants in the aqueous phase. In order to synthesized the ZnO-petcoke composite, the petcoke was stabilized previously to its addition to the ZnO precursor solution. ZnO-petcoke composites were characterized with different spectrophotometric and physicochemical techniques and evaluated in the photodegradation reaction of methyl orange. The ZnO supported with petcoke thermally stabilized was the composite with the best degradation performance reaching a 30% higher removal efficiency than unsupported ZnO. The results indicated that it is possible to revalorize petcoke materials as carbon additives for improving the photocatalytic performance of semiconductors. Simple thermal annealing is enough for creating stable materials with improved pollutant removal capacities.

Graphic Abstract

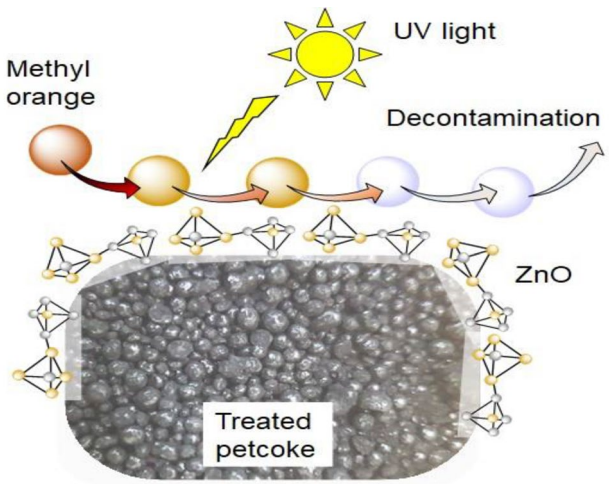

Keywords Petcoke · ZnO · Photocatalyst · Composite · Revalorization

Statement of Novelty

This manuscript addresses the potential revalorization of the petcoke, waste from the petrochemical industry, to be used as a support for photocatalysis semiconductors to improve its physicochemical properties and degradation capabilities treating recalcitrant dye pollutants. The manuscript presents the methodology and results of the synthesis and

✉ J. O. Saucedo-Lucero
jsaucedo@ciatec.mx; j.octavio.saucedo@gmail.com

[1] CIATEC A.C. Centro de Innovación Aplicada en Tecnología Competitiva, Omega 201, Industrial Delta, León 37545, GTO, México

[2] CONACYT-CIATEC A.C. Centro de Innovación Aplicada en Tecnologías Competitivas, Omega 201, Industrial Delta, León 37545, GTO, México

Published online: 24 September 2021

characterization for ZnO/petcoke composites and its photocatalytic activity evaluation for the removal of a model pollutant molecule in the aqueous phase. To the best of the author's knowledge, this is the first research work in which petcoke treatment residues are being employed as a matrix for the deposition of ZnO and be employed as decontamination media. Thus, the present represents a considerable contribution to material science and sustainable development.

Introduction

Petcoke is solid material of high carbon content obtained from crude petroleum in refineries. It is a residue of petroleum oil's thermal cracking. It consists of heavy fractions of hydrocarbons with significant sulfur and nitrogen impurities and trace concentrations of heavy metals, mainly vanadium and nickel (composition might change depending on the precedence of the petroleum) [1]. Traditionally, petcoke has been employed as a fuel in cement kilns, combustion plants, and electrodes for metal refining. Petcoke burning releases detrimental byproducts, such as SO_x and NO_x gases, among other hazardous compounds [2, 3]. Furthermore, petcoke combustion traditionally produces more CO_2 per mass unit than other fuels (102.1 kg/BTU) [4], making it one of the principal contributors to climate change. For these reasons, several environmental agencies had stringent environmental regulations limiting the use of petcoke as fuel (e.g., the European Union requires favors the consumption of renewable fuels over fossil-based, as part of their energetic goal for 2030 [5]). Recent geopolitical changes of the modern world are causing increased consumption and exploitation of petroleum. This, combined with crude oils becoming heavier despite the current market demand for light fuels, results in few applications for petcoke.

Recently, novel methodologies for petcoke revalorization have been developed and successfully employed. Some of them include: use as adducts in construction materials [6], its conversion by co-gasification or co-combustion [7, 8], transformation to metallurgical coke [9], a precursor for activated carbon production [10], among others. Due to their high carbon content and relative chemical stability (not accounting for sulfur compounds), petcoke can also be employed as material support to deposition active metal oxides for catalytic/photocatalytic applications. However, the presence of soluble impurities, most of all sulfur, might hinder their application. A thermal stabilization to desorb volatile and semi-volatile organic compounds and surface sulfur impurities, followed by an acidic treatment to remove inorganic impurities, could result in the proper stabilization of petcoke applications as photo/catalytic support.

On the other hand, tons of new industrial compounds are being produced and sometimes released into the ecosystems every year. Surface water is particularly susceptible to being polluted, as it often is the final destination of industrial wastewater. The textile industry releases a considerable amount of wastewater contaminated with hazardous dyes. Azo-based are of utmost importance since they can possess toxic properties and sometimes be carcinogenic either by themselves or their natural degradation products [11]. For that reason, advanced physicochemical processes are required in order to mineralize or reduce its toxicity ultimately. Photocatalytic-driven advanced oxidation is a process suitable for the advanced treatment of azo dyes [12]. The process involves using semiconductor materials that, upon UV/Vis irradiation, can produce free radicals. In recent years, a large effort to develop materials with the capacity of degrading azo dyes [13, 14]. They are of utmost importance to ensure water systems' health and because their recalcitrant nature usually represents the controlling compound for designing advanced water treatments.

Zinc oxide is a semiconductor with a band gap (Eg) of 3.37 that can be modified in an extensive range (between 2.3 and 4) by several strategies, including the formation of composites [15–17]. The research has been intensified every time, in one part since it represents a suitable alternative to TiO_2, due to its high quantum yield and superior catalytic efficiencies [12, 18], and another part for its better adsorption performance and resistance to photocorrosion [19]. Early studies have reported a synergy of carbon combination with semiconductors [20, 21], such as improvements in the adsorption capacity of by-products, resistance to poisoning, and their degradation capacities. This effect has been reported even for carbons of low surface area in which adsorption occurs fast. The particular behavior of composite material also depends on the carbon´s specific features, including surface chemistry and pore structure linked to their carbonization temperatures [22].

The focus of the current study is to employ chemically and thermally treated petcoke as support for ZnO deposition and their performance to remove a model azo dye from an aqueous solution such as methylene orange. Two approaches were employed to stabilize the petcoke: (1) thermal annealing alone and followed by (2) chemical acidification. The purpose of the treatments was to remove organic and inorganic compounds from petcoke to obtain a carbon-rich material.

Materials and Methods

Chemicals

All chemicals employed were of analytical grade: HNO_3, $ZnCl_2$, sodium dodecyl sulfate (SDS), NaOH 0.1 M

(certified solution by Baker), $NaNO_3$, methyl orange (MO). Green petroleum coke was provided by Carbones DC.

Treatment of Petcoke

The petcoke was milled, sieved (< 250 µm), and dried at 100 °C for 2 h. Then, it was heated at 5 °C/min to 250 °C and annealed in static air for 5 h. The annealed petcoke was cooled at room temperature inside a desiccant capsule; this material was named C. After cooling, an additional acid treatment was carried out after cooling, undergoing HNO_3 (30% vol.) reflux at 60 °C for 6 h. The solids were recovered by decantation, washed with deionized water until pH 4 was reached, and finally, drying overnight at 100 °C; this material was named C–H.

Synthesis of Petcoke-ZnO Composites

In a beaker, 600 mL of a $ZnCl_2$ solution (0.0493 M) was mixed with 25 mL of SDS (0.01 M). The mixture was stirred for 30 min, and then 1 g of the petcoke was added to the solution and stirred for extra 30 min. During this stirring time, an aqueous solution of 0.1 M NaOH was slowly dropped with the assistance of an automatic titration machine (T15, Metrohom) at a rate of 1 mL/min, up to 82 mL. The suspension was filtered in a vacuum system, using a membrane of 0.45 µm. The solid was rinsed several times with deionized water up to neutral pH until no zinc or chloride was detected in the rinsing solution. The obtained solid was dried at 95 °C for 24 h, and then it was calcined at 250 °C for 4 h. Finally, the resulting material was characterized and tested for photocatalytic activity.

Materials Characterization

Gravimetric Characterization

Gravimetric analysis was performed to calculate the apparent density of the materials. From here, it was possible to calculate the impregnation degree (ID) of the ZnO over the petcoke (treated and untreated) through differences in the mass of the materials in a given volume. Both values were necessary to determine the amount of photoactive material added in the photocatalytic tests.

Chemical Stability

The synthesized materials were tested for chemical stability under various pH conditions. For this, 1 g of solid was contacted with 20 mL of an aqueous solution at different pH values (3, 5, 7, or 9) into vials. HCl (0.1 M) and KOH (1.0 M) solutions were used as pH regulators. The vials were closed and keep under constant stirring for 24 h. Later, the solution was membrane filtered and then analyzed for zinc content using an atomic absorption spectrometer (Thermo).

X-Ray Diffraction (XRD)

X-Ray diffraction (XRD) data were performed using a Bruker D8 Advance powder diffractometer provided with graphite monochromator and filtered Cu Kα radiation at 30 kV acceleration and 10 mA current (λ = 0.154178 nm). The diffractograms were collected between 10–80°. Data acquisition and phase identification were performed with DIFFRAC.SUITE software, using ICDD-PDF reference database.

Fourier Transform- Infrared Spectroscopy (FT-IR)

Fourier Transform Infrared Spectroscopy was obtained in a Nicolet iS 10 (Thermo) operated in Attenuated Total Reflectance mode. Classical corrections for atmospheric humidity and CO_2 were applied. Each spectrum was formed by an average of 32 scans with a resolution of 4 cm^{-1}.

Potentiometric Titration

Potentiometric titration experiments were carried out in a 916 Ti-touch from Metrohom. The procedure is reported elsewhere [23]. The surface charge distribution was calculated as the amount of protons adsorbed/released from the surface with the formula:

$$Q = \frac{1}{m}\left[V_0\left\{H_s - OH_s\right\} + V_t N_t - \left(V_0 + V_t\right)\left\{H_f - OH_f\right\}\right] \quad (1)$$

where Q is the amount of adsorbed or released protons from the surface (addresses as surface charge), V_0 and V_t are the solutions, and titrant volumes added, N_t is the normality of titrant, m is the titrated mass, and the suffixes s and f stand for the starting and final concentrations of H^+ and OH^- ions by using the Davies equation [24].

Nitrogen Physisorption

Nitrogen physisorption at 77 K determined the textural properties of the synthesized materials. The experiments were carried on a Tristar II Micromeritics apparatus using samples degassed ($< 10^{-5}$ Pa) at 473 K for 2.0 h. The surface area (S_{BET}) was obtained from adsorption isotherm data for the monolayer ($0.10 < P/P_0 > 0.30$) using the multi-point Brunauer–Emmett–Teller (BET) method ([25], Eq. 2).

$$\frac{P/P_0}{V(1 - P/P_0)} = \frac{1}{V_m C} + \frac{C - 1}{V_m C}(P/P_0) \quad (2)$$

where V is the specific volume adsorbed at the relative pressure P/P_0, V_m is the specific monolayer capacity, and the

parameter C *is* related to the energy of monolayer adsorption. The pore size distribution was determined from the desorption isotherm by the Barrett-Joyner-Halenda (BJH) method [26]. Total pore volume was determined from the N_2-adsorption point at $P/P_0 \sim 1$.

Diffuse Reflectance

Diffuse Reflectance spectra were recorded in reflectance function mode (Eq. 3) between 200 and 500 nm, with Cary 4000 Agilent spectrometer equipped with a praying mantis diffuse reflectance accessory. A Spectralon 99% reflectance standard was used as a reference.

$$F(R_\infty) = \frac{(1-R_\infty)^2}{2R_\infty} \tag{3}$$

The band gap energy (Eg) for the synthesized materials was estimated from the modified Kubelka–Munk function (Eq. 4) using Tauc plots [27].

$$(F(R_\infty) \cdot h\nu)^{1/n} = B(h\nu - Eg) \tag{4}$$

where R_∞ is the reflectance of the infinitely thick specimen, *h* is the Plank constant, ν is the photon' frequency, and B is a proportionality factor. The *n* factor depends on the nature of the electron transition and is equal to 1/2 or 2 for direct or indirect transition band gaps, respectively.

Microscopy Analysis

Scanning electron microscopy (SEM) was used to analyze the surface morphology of the synthesized materials by an FEI HELIOS NANOLAB 600 scanning electron microscopy equipped with an energy-dispersive X-Ray (EDS) apparatus to determine element composition on the surface of the samples. The samples were first dispersed in absolute ethanol, deposited on copper grids, and dried.

Dark Adsorption Isotherms

Adsorption isotherms were carried out in dark conditions. A mass of about 0.1 g of each material was contacted with 20 mL of a solution containing a specific concentration of Methyl Orange (MO) in a centrifuge vial. The vial was covered with aluminum foil and keep in a dark room in a stirred water bath at 25 °C. The experiments were adjusted to pH 9 by the daily additions of 0.01 M NaOH or 0.01 M HCl. Special care was taken to keep the experiments in the absence of light. After 3 days of equilibrium, the solutions were centrifuged, and an aliquot of 5 mL was sampled for analysis. Dye analysis was carried out in a UV–Vis spectrometer (Evolution 300, Thermo) at a wavelength of 466 nm (maximum adsorption wavelength, obtained experimentally). The adsorption capacity was calculated by making a mass balance in the reaction and considering that all MO has been transferred from the solution to the solid without undergoing decomposition. The mass balance is:

$$Q_{eq} = \frac{V(C_{eq} - C_0)}{m} \tag{5}$$

where Q_{eq} is the adsorption capacity, expressed as mass (or mole) of the dye per gram of adsorbent, reached at the equilibrium concentration C_{eq} in mg/L or µmol/L; C_0 is the starting dye concentration, and mass is the adsorbent mass in g. In order to evaluate the mechanism of dark adsorption on MO in ZnO + petcoke composites, the following experiment was designed. 0.1 g of each material was contacted with 25 mL of a solution of 30 mg/L of MO pH of 7.14. The containers were covered with aluminum foil and keep in the dark for 24 h. After the liquid was filtered and the solid adsorbent was dried at 100 °C for 24 h. After that time, the material was analyzed by FT-IR.

Photocatalytic Degradation Tests

Photocatalytic degradation tests were carried out in a 300 mL batch quartz reactor containing a water recirculation system to control the temperature of the reaction mixture and a UV light lamp ($\lambda = 254$ nm and $I = 0.09$ mW/cm^2) located in the center of the reactor (Fig. 1).

A mass of 0.5 g supported material (ZnO + petcoke) was added to a 250 mL of MO solution (30 ppm at pH 9.0) for its photocatalytic evaluation under UV light irradiation. Before catalytic evaluation, the materials were kept in contact with the reaction solution for one hour in complete darkness, and vigorous stirring reaches an adsorption

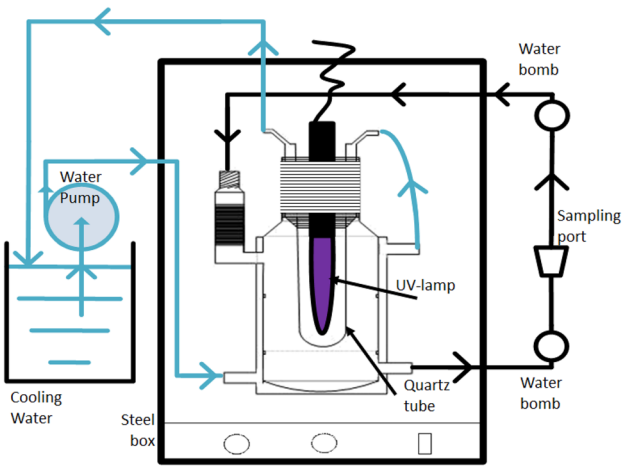

Fig. 1 Scheme of the photoreactor employed

equilibrium. After, the lamp was turned on for 40 min, where 0.3 mL aliquots were taken every 3 min to monitor MO´s concentration. Photolysis blanks were made following the same procedure without the catalyst material. All tests were done in triplicate, average and standard error were calculated.

Results and Discussions

Material Characterization

Gravimetric Characterization

The results of the gravimetric analysis are summarized in Table 1. The increase in the mass given a specific volume (1.0 mL) is directly associated with the increase in the petcoke amount impregnated over the ZnO powder. In this case, C–ZnO has an impregnation degree of 0.908 $g_{ZnO}/g_{C\text{-}ZnO,}$ while C–H–ZnO registered a value of 0.865 $g_{ZnO}/g_{C–H–ZnO}$. These values allow to determining the amount of photoactive material that was present in the MO degradation tests, which were 0.454 g and 0.432 g for C–ZnO and Z–H–ZnO, respectively.

Chemical Stability Experiments

In order to verify the stability of the materials upon different pHs, these were subject to leaching with solutions of different pHs. The amount of total Zn leached from the surface is provided in Fig. 2. The leaching percentages were calculated by the total zinc mass present in each of the materials. As can be seen, as the pH decreases, there is an increase of zinc dissolved, higher in the C–ZnO. Highest Zn dissolution was observed in C–ZnO; this is probably due to the remaining unbounded Zn ions left from the synthesis. At pH > 3, the highest stability was observed in the material C–H–ZnO, suggesting protection of the particle by the acidic treated petcoke. Notwithstanding this, most of the materials had a leaching percentage of less than 2%, corroborating the high stability of the materials even at acidic conditions.

Table 1 Gravimetric characterization of ZnO materials

Material	Apparent density (g/mL)	Impregnation degree ($g_{ZnO}/g_{C–ZnO}$)	Amount of photoactive material per test (g)
ZnO	0.629	N.A	0.500
C–ZnO	0.699	0.908	0.454
C–H–ZnO	0.727	0.865	0.432

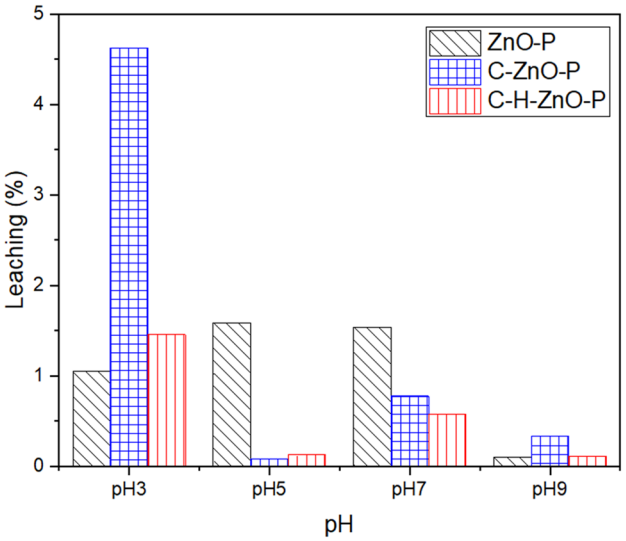

Fig. 2 Zinc leaching percentage of the studied materials

X-Ray Diffraction

The X-Ray diffractograms of the synthesized materials are shown in Fig. 3, while the crystal parameters are in Table 2. All samples showed well-resolved diffraction peaks at the position of 31.8, 34.4, 36.3, 47.5, 56.6, 62.9, 66.4, 68.0, 69.1,72.6, and 77.0° in 2-theta, which are in agreement with the reflections of (100), (002), (101), (102), (110), (103), (200), (112), (201), (004), and (202) planes of P63mc

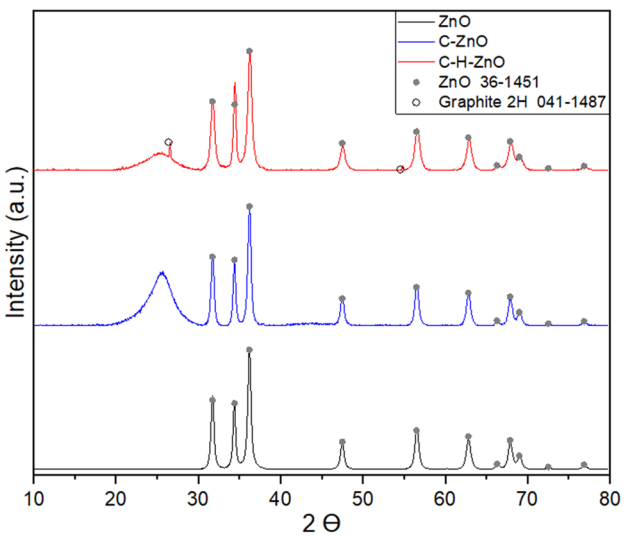

Fig. 3 X-Ray Diffraction Patterns of the synthesized materials

Table 2 Cristal structure parameters of the studied materials

Material	Crystalline structure	Crystallite size (nm)
ZnO	h-ZnO	20
C–ZnO	h–ZnO	21
	Graphite	–
C–H–ZnO	h–ZnO	21
	Graphite	–

hexagonal symmetry, distinctive of wurtzite structure of ZnO (JCPDS 36-1451) [28].

Unlike the ZnO sample, the C–ZnO and C–H–ZnO samples showed a set of broadband centered at 26.4° and a weaker peak between 44.5° assigned to the (002) and (110)/(101) planes of intermediate structures between graphene-2 H (PDF: 00-041-1487) and the amorphous state (random layer lattice structure). Also, the C–H–ZnO spectrum shows sharp diffraction peaks at 26.7 and 55.0° assigned to (002) and (004) planes associated with graphite (JCPDS 01-075-2078), suggesting that the acidic treatment of petcoke exposed occluded crystalline graphite particles.

FT-IR Characterization

The FT-IR spectra are displayed in Fig. 4. Pure zinc oxide has a wide band centered at 3503 cm^{-1} attributed to bulk –OH groups, whereas a band at 553 cm^{-1} was attributed to the vibration of Zn–O [29]. The bands located at 2981 and 912 cm^{-1} can be ascribed as SDS leftover impurities [30].

On the other hand, supported ZnO materials demonstrated a similar FT-IR pattern with subtle differences. For example, in the ZnO, the OH groups' band was slightly shifted to 3487 and 1338 cm^{-1} for C–ZnO and C–H–ZnO, respectively. This is a very well-known effect of change in the environment of hydroxyl groups, which is probably distorted due to coordination of the inner complex with the zinc oxide/hydroxide [31]. When zinc oxyhydroxides are contacted with the surface of C–H, there is an adsorption of zinc ions over dissociated carboxyl groups. The SDS surrounds the adsorbed complexes and, upon an increase in the pH value, blocks coordination groups limiting the olation and hydroxylation of zinc. As a result, there is particle condensation at smaller sizes, and because of the inner sphere coordination of zinc, there is also a stronger bond between the carbon matrix and the zinc oxide.

Surface Charge Distribution

The surface charge distributions, measured as protons released from the surface, are displayed in Fig. 5. Even though FT-IR measurements demonstrated differences in the surface chemistry of both pristine ZnO, the charge distribution demonstrated that at least, in terms of surface acidity, both materials behaved in a similar similarly, with slightly more acidity in ZnO. In both cases, matrix presence results in an increase in the pH value for point of zero charge (pH-PZC) from 8.0 (ZnO) to 8.6 (C–ZnO) and 8.8 (C–H–ZnO) in modified materials. This is an expected result since some of the most acidic sites of the zinc oxide (terminal oxygenated) are now interacting with the surface of the carbon materials, therefore, not allowing for proton adsorption. It is interesting to notice that the particular shape of the proton binding

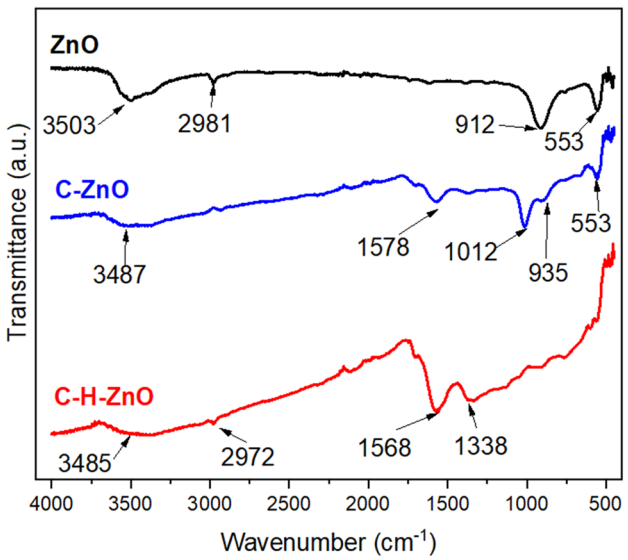

Fig. 4 FT-IR in the ATR mode of the synthesized materials

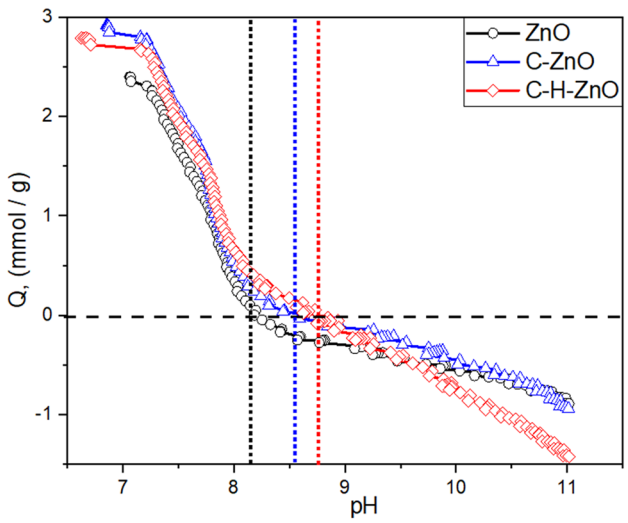

Fig. 5 Surface charge distribution of studied materials, the intersection of the *x*-axis (pH-PZC) is located with dotted lines

Table 3 BET surface area and pore size and volume of ZnO and hybrid C–H–ZnO material

Material	S^{BET} (m^2/g)	Total pore volume (cm^3/g)	Average pore size (nm)
ZnO	20.0	0.218	43.3
C–H–ZnO	6.00	0.015	9.6

isotherm was not affected by the presence of the carbon matrixes. This suggests that no new moieties are being created on the composite material but rather a redistribution of the pKa's surface groups. It is expected that such change on the pKa of surface groups will be reflected in how adsorbent molecules are adsorbed and transformed on the material's surface.

Surface BET Area and Pore Size Distribution

The S_{BET} and pore volume measurements of ZnO and C–H–ZnO are summarized in Table 3, whereas N_2 physisorption isotherms and pore size distribution are displayed in Figure S1 (Supplementary Information S1). According to the IUPAC classification [25], the materials showed type-IV(a) isotherm with type-H3 hysteresis loop typical to ZnO mesoporous. In this case, the specific surface area was higher in the pure ZnO than C–H–ZnO composite material. This result was consistent with other characterization reports over sol–gel zinc oxide [19]. This decrease is related to the composites' mechanisms´ formation and the low surface of petcoke. The change in pore size distribution (inserts in Figure S1) suggested filling pores of about 50 nm on ZnO, leaving to mesopores of about 10 nm (in the C–H–ZnO). This shift in the porosity might be significant in terms of adsorption of the selected dye. Methyl orange has a size of about $1.20 \times 0.68 \times 0.37$ nm [32]; thus can penetrate C–H–ZnO pores. However, during the test, most of the pore volume collapsed, decreasing the adsorption capacity. On the other hand, this pore constriction might improve transport across the pores, improving adsorption kinetics.

UV–Vis Diffuse Reflectance

Figure 6 shows the UV–Vis diffuse reflectance spectra and Tauc plots for direct and indirect bandgap semiconductors. UV–Vis spectra show characteristic reflectance function curves with adsorption edges between 390 and 410 nm (Fig. 6a). The region showing a steep, linear increase of light absorption with increasing energy is characteristic of semiconductor materials. The *x*-axis intersection point of the linear fit of the Tauc plot gives an estimate of the band gap energy.

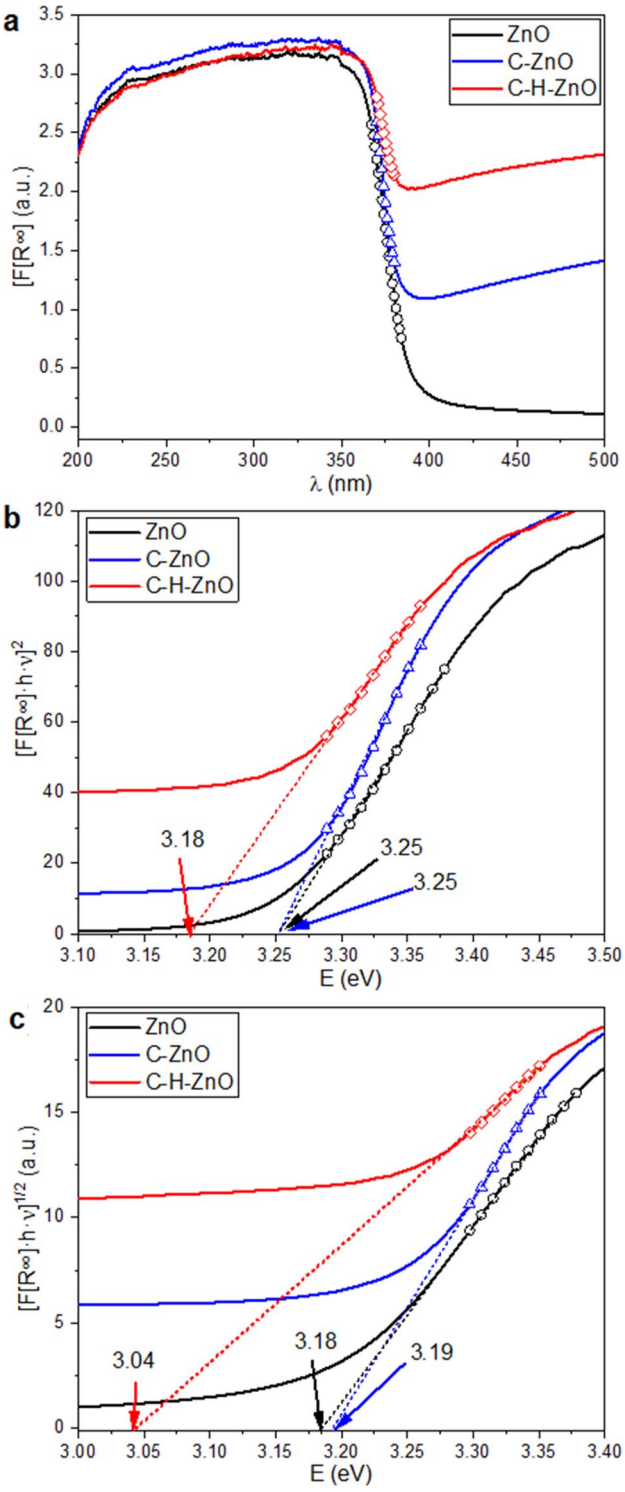

Fig. 6 **a** Original UV–Vis diffuse reflectance of ZnO, C–Zn–O and C–H–ZnO; Kubelka–Munk for **b** direct and **c** indirect optical Band Gap of materials

Both direct and indirect bandgap energies (Eg) of ZnO particles were estimated by the *x*-axis intersection point of the linear fit of the Tauc plot (Fig. 6b, c). The direct bandgap

values were 3.25 eV for both ZnO and C–ZnO and 3.18 eV for C–H–ZnO. The indirect bandgap value was 3.04 for C–H–ZnO and 3.19 eV for both ZnO and C–ZnO. Thus, the carbonaceous support's acid treatment caused a significant shift of the bandgap energy toward the visible light region. In contrast, it did not influence the ZnO particles bandgap when considering the support without acid treatment.

Microscopy Analysis

Figure 7 shows the SEM images and EDX analysis for the synthesized C–ZnO and C–H–ZnO composites. The EDS analyzes reveal that C, S, O, and Zn are the main constituent of the synthesized materials. The micrographs show that both C–ZnO and C–H–ZnO materials are composed

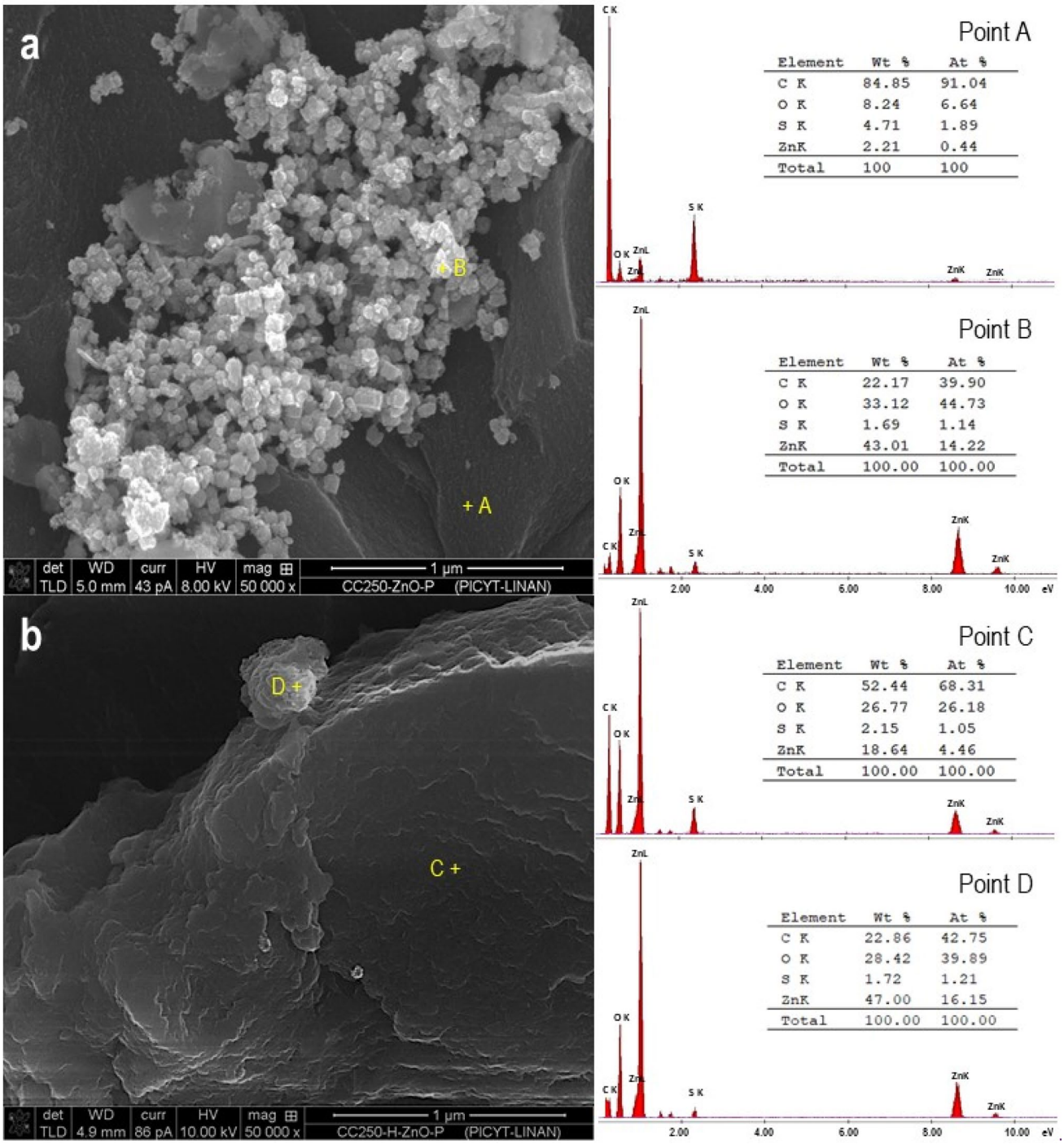

Fig. 7 Scanning electron micrographs image and EDX analyses of the surface for **a** C-ZnO and **b** C–H–ZnO composites

of two segregated phases: (1) carbonaceous phase formed for a regular pattern and compact surface without visible porous areas; and another (2) composed by a set of like spherical ZnO nanoparticles with a relatively homogeneous size distribution, aggregated and generating larger particles. The ZnO-nanoparticles size obtained from SEM images (24 ± 8 nm) was consistent with the Scherrer calculations (21 nm; Table 2).

EDS analyses evidenced significant composition differences between carbonaceous phases in C–ZnO and C–H–ZnO samples. In this sense, the C–H–ZnO sample showed 4- and 10-fold more oxygen and zinc (point C) than the C–ZnO sample (point A). Such differences would be related to the petcoke surface functionalization with oxygenated groups due to acid treatment, as evidenced by FT-IR characterization, favoring the electrostatic interaction between the oxygenated surface groups and Zn ions during the impregnation step and improving the ZnO phase dispersion on the carbonaceous surface. The surface composition of the ZnO clusters was consistent in both materials (points B and C).

Adsorption Isotherms

Adsorption isotherms were obtained to determine the behavior of the MO upon contact with the materials. The adsorption isotherms were adjusted to the Langmuir equation:

$$Q = \frac{Q_{\max} \times b \times C_{eq}}{1 + b \times C_{eq}} \quad (6)$$

where Q (mg/g) is the adsorption capacity at the equilibrium concentration C_{eq} (mg/L), Q_{max} (mg/g) represents the maximum adsorption capacity and therefore the capacity of the monolayer, and b is the Langmuir constant (L/mg). Isotherms are provided in Fig. 8, and the results of the fitting in Table 4.

The total number of adsorption sites of MO was not affected by the presence of annealed coke, which is interesting because this material has 50% of ZnO, and it is expected that the capacity drops at least in this amount.

The fact is that ZnO's adsorption capacity in dark conditions was low, therefore few differences between both materials were appreciated. On the other hand, acidified coke indeed promoted the adsorption of MO. As mentioned in the experimental characterization, the insertion of acidic oxygen groups affects the surface charge distribution. Methyl Orange is a color indicator with a pK_a of about 3.47. At the adsorption pH of 9, MO is wholly dissociated and is being repelled from the surface of the carbons. Since C–H–ZnO had the highest acidic surface, the higher adsorption capacity can be explained by interaction with protonated sites such as the dimethyl alanine and π–π* interactions between the aromatic ring carbon and the dye. Nonetheless, the adsorption capacity of the materials was unfavorable; the maximum capacity reached experimentally on the best material was lower than 2.5 mg/g up to concentrations higher than 80 mg/L. Hence, MO removal can be attributed mainly to photocatalysis rather than adsorption.

In order to understand the primary mechanism of MO adsorption on the composite materials, we saturated their surface under dark conditions and then analyzed it by FT-IR. The Figures are provided in the Supplementary Information S2. After adsorption, there is a shift of bands related to

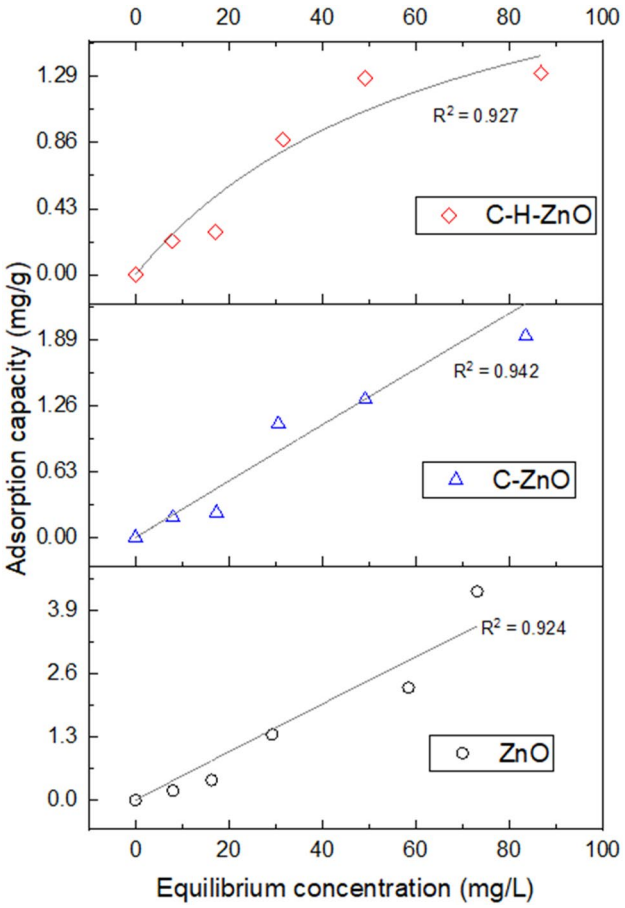

Fig. 8 Methyl orange dark adsorption isotherms in dark condition at pH 9 and 25 °C. Equilibrium time of 5 days. The lines correspond to the Langmuir adsorption model

Table 4 Results of the adsorption fitting to the Langmuir adsorption model

Material	Q_{max} (mg/g)	b (L/mg)	R^2
ZnO	172.4	0.000294	0.968
C–ZnO	172.4	0.000158	0.940
C–H–ZnO	2.55	0.0146	0.949

hydroxyl and carbonyl groups, suggesting carboxylic groups' involvement during adsorption, similarly to the reported in activated carbon [33]. The results suggest the electrostatically driven adsorption occurring between MO and negatively charged hydroxyl groups. Since the surface was actually positively charged at the adsorption pH, uptake occurred only in located sites of the surface, therefore explaining the low capacity determined. Most likely, the presence of terminal and bridging oxygen groups of zinc oxide contributes to the adsorption. No evidence of π–π* interactions was observed, probably because most of the coke surface was covered by ZnO as observed in SEM analysis.

Photocatalytic Degradation Tests

The photocatalytic activity of the materials was tested during the degradation of MO, and profiles are shown in Fig. 9. The first to notice is that the ZnO materials displayed a photocatalytic activity greater than photolysis. On the other hand, photolysis only reached a removal amount of 50.1% within 40 min that the tests lasted, while the impregnated ZnO materials reached removal rates above 70% (77.1 and 72.5% for C–ZnO and C–H–ZnO, respectively). The exception was the unmodified ZnO, which only achieve a degradation rate of 61% during the UV irradiation period.

By the Langmuir–Hinshelwood kinetics model, the photocatalytic degradation process of methyl orange dye can be expressed as apparent pseudo-first-order kinetic (Eq. 3).

$$-Ln\left(C/C_0\right) = k_{APP} \times t \tag{7}$$

where k_{APP} is the apparent pseudo-first-order rate constant, C_0 is the initial MO concentration, and C is the MO concentration at time t. The slope obtained by graphing $-Ln(C/C_0)$ vs. t could provide the value of k for each material (Fig. 8b), and the coefficient of determination (r^2) can ensure the linear fit of the curves of each degradation test.

In our case, all the lineal adjustment of the photodegradation process (including photolysis) registered an r^2 value over 0.98, indicating a good fit of the Langmuir–Hinshelwood kinetics model with photocatalytic performance directly proportional to k_{APP}. It is important to mention that k_{APP} value encloses two simultaneous and independent phenomena: direct photolysis and free radical degradation. In this case, the photocatalytic rate constant value ($k_{OH\cdot}$) determination can be obtained by the difference between the constant rate value of the photolysis (k_{UV}) and k_{APP}. After then,

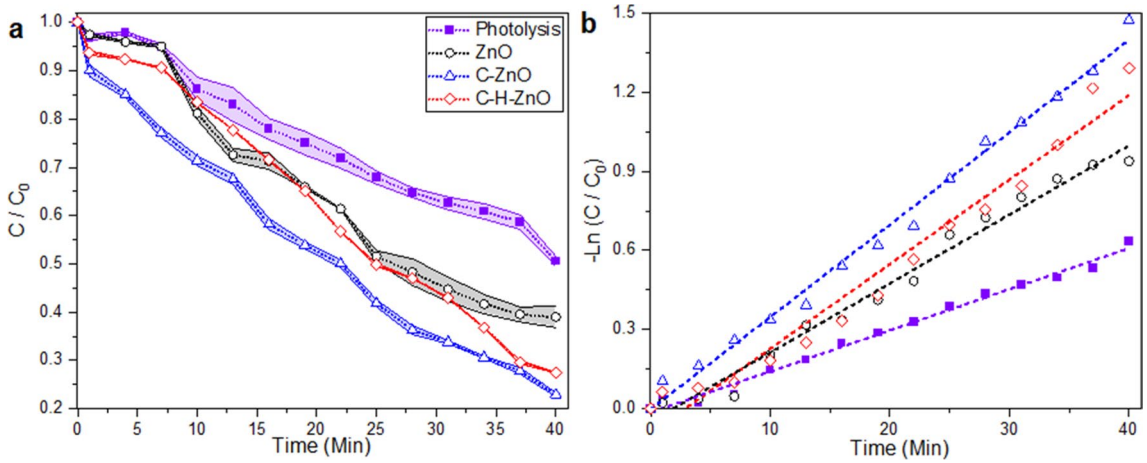

Fig. 9 Photo-assisted degradation of methyl orange. **a** Photocatalytic activity of de ZnO-Based materials. **b** Lineal adjustment of the photodegradation process

Table 5 Photodegradation apparent pseudo-first order rate constants

Material	k_{app} ($\times 10^{-2}$ min^{-1})	$k_{OH\cdot}$ ($\times 10^{-2}$ min^{-1})	% TPC* Photocatalyst	% TPC* photolysis	SDR** (g_{MO} / g_{ZnO} min)
ZnO	2.6	1.1	42.30	57.69	0.352
C–ZnO	3.5	2.0	57.14	42.85	0.364
C–H–ZnO	3.4	1.9	55.88	44.11	0.371

**TPC* total photodegradation contribution

***SDR* Specific degradation rate. $\boldsymbol{k_{UV} = 1.5 \times 10^{-2}\ min^{-1}}$

the contribution percentage for each photo-assisted degradation process can be determined. Table 5 summarized the k_{app}, $k_{UV,}$ and $k_{OH^{\cdot}}$ values determined for each material and the percentages of MO degradation contribution.

The first thing to note is that all the materials have k_{APP} higher than the k_{UV}, so all the ZnO-based material shows a photocatalytic activity to a lesser or greater extent. While direct photolysis achieves a k_{UV} of 0.015 min^{-1}, the ZnO-based material reported values of k_{APP} of 0.034, 0.035, and 0.026 min^{-1} for C–H–ZnO, C–ZnO, and ZnO, respectively. After comparing the values of k_{APP}, it can be stated that the coke doping of ZnO improves the MO degradation by increasing the photocatalytic contribution above 55% of the total photodegradation contribution.

However, to make a fairer comparison regarding the degradation capacity of the materials, and knowing in advance that the amount of photocatalytic material was not the same for each test (Table 1), it was necessary to calculate the specific degradation rate for each ZnO-based material (Table 5). The first thing to observe is that C–H–ZnO is the material with the highest methyl orange degradation rate, this when registering values of 0.371 g_{MO}/g_{ZnO} min, followed by both material without acid treatment (C–ZnO) and the pure ZnO (0.364 and 0.352 g_{MO}/g_{ZnO} min, respectively). So, despite C–H–ZnO reached removal capacities similar or superior at those materials without acid treatment nor impregnation. Table 6 contains a comparison with highlighted similar works available in the literature dealing with Methyl Orange removal. A direct comparison in terms of performance is complicated since most authors define their reaction systems and conditions. When comparing kinetic constant, the materials presented here performed lower than other porous synthetic materials like Ag–N–ZnO-Activated Carbon but higher than others like TiO_2-AC composites and ZnO-graphene composites.

Degradation Mechanism

Based on the photocatalytic degradation results, it could be inferred that the methyl orange degradation mechanism followed the path proposed by Gamarra et al. [40] (Fig. 10).

This proposed photocatalytic degradation mechanism consist first on the breaking of the azo bond, and the subsequent breaking of the aromatic rings producing organic intermediates such as nitrobenzene, phenol, 1,4-benzoquinone, until its complete mineralization to CO_2 and H_2O. Despite the proposed pathway could be applied, this mechanism is theoretical, so more studies are required to monitor the specific degradation by-products and establish a mechanism for this material.

Conclusions

The present manuscript demonstrated that it is possible to revalorize petcoke as a precursor material for the synthesis of hybrid ZnO-carbon semiconductor materials and be employed to remove a model colorant dye from an aqueous solution. The results suggest forming a stable composite material in which electrostatic interactions between the

Table 6 Highlighted studies on the literature related to methyl orange removal by different photocatalysts

Material	Conditions	Results	Authors
Ag–N–ZnO supported in different activated carbons	25 °C, C_i of 30 mg/L, a wavelength of 420 nm	98, 90 and 80% removal in 120 min; $K_1 = 0.396$, 0.366, and 0.273 min^{-1}, for coconut-husk, coal and almond activated carbons respectively	[34]
Pristine ZnO and grafene-ZnO composite	C_i of 5×10^{-5} M, solar light	52 and 97% removal in 120 min. $K_1 = 0.008$ and 0.024 min^{-1}. For ZnO and Gr–ZnO composite respectively	[35]
ZnO-Carbon aerogel composite	25 °C, homemade lamp of 420 nm wavelength	$K_1 = 0.321$ min^{-1}	[36]
Ternary composite made of ZnO/rGO/PAN	$C_i = 10$ mg/L, Hg lamp	99% removal in 60 min. (no kinetic adjustments were carried out)	[37]
TiO_2-AC composite	$C_i = 50$ mg/L, visible light lamp and solar irradiation (in a cylindrical concentrator)	94.2 and 98.6% removal in 180 min, $K_1 = 0.017$ and 0.0231 min^{-1} for peachstone activated carbon under visible lamp and solar irradiation respectively.	[38]
ZnO- carbon spheres (obtained with CVD) composite	$C_i = 10$ mg/L, a wavelength of 365 nm	87% removal in 180 min, $K_1 = 0.010$ min^{-1}	[39]
Thermally and chemically treated coke-ZnO composites	$C_i = 30$ mg/L, wavelength of 254 nm	77.1 and 72.5% in 40 min, $K_1 = 0.035$ and 0.034 min^{-1} for C–ZnO and C–H–ZnO composites respectively	This work

K_1 stands for the kinetic constant of pseudo-first-order

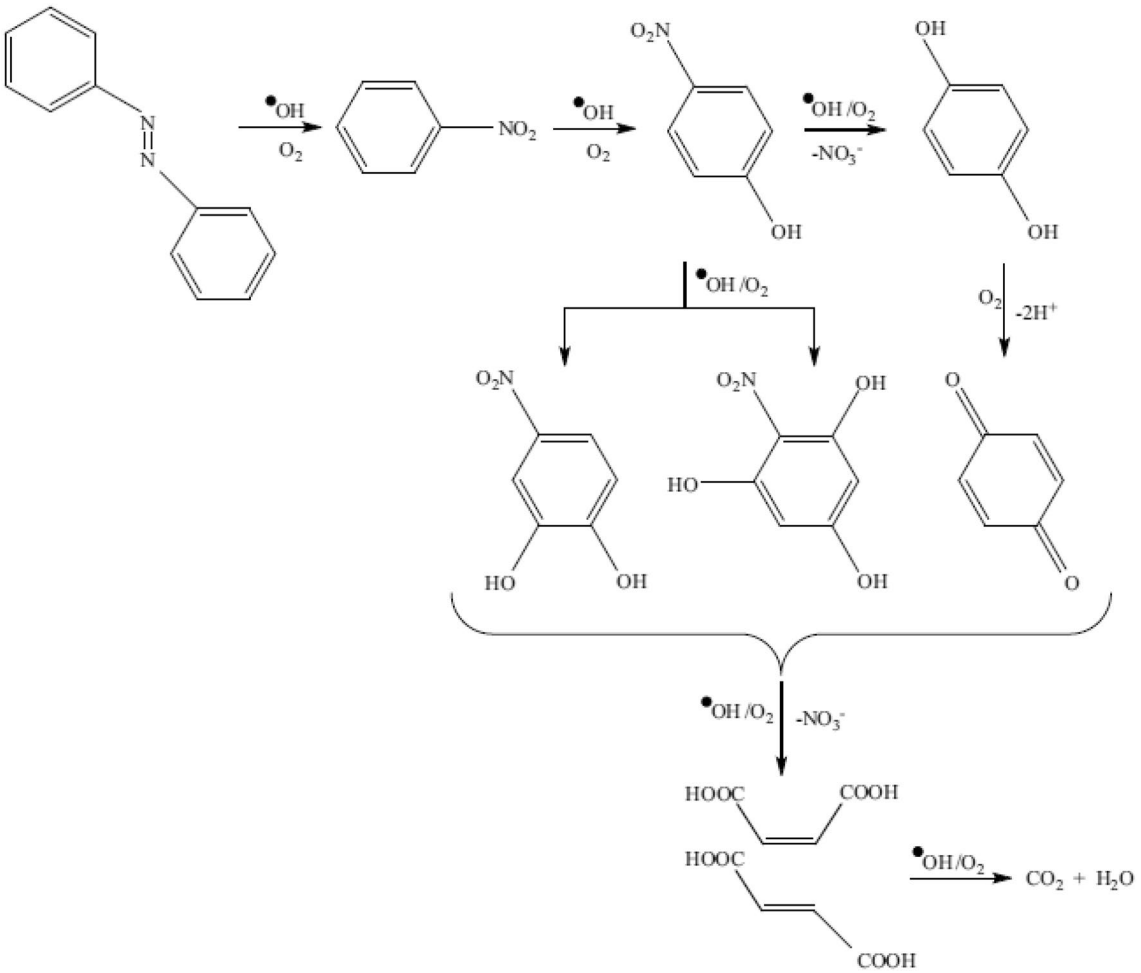

Fig. 10 Methyl orange dye theoretical photocatalytic degradation mechanism by Gamarra et al. [40]

carbon surface´s groups and zinc hydroxide groups occur. Upon carbon oxidation, there is a strong covalent bond formation between carboxylic groups and terminal hydroxyl groups. However, such strong interaction represents a decrease in available oxygen groups and a lower surface area, which does not represent a considerable improvement of the photocatalytic behavior of the ZnO. On the other hand, the petcoke that was only thermally stabilized considerably improved the chemical stability and enhanced ZnO's performance. Under dark conditions, the materials displayed a low adsorption capacity, and upon UV-irradiation, the dye was efficiently removed. The best performance was observed in C–ZnO, in which 80% of degradation was reached in 40 min; this result represented an improvement around 33% greater than ZnO performance (60% degradation). The results indicated that it is possible to revalorize petcoke materials as carbon additives for improving the photocatalytic performance of semiconductors. Simple thermal annealing is enough for creating stable materials with improved pollutant removal capacities.

Supplementary Information The online version contains supplementary material available at https://doi.org/10.1007/s12649-021-01585-w.

Acknowledgements Thanks for the financial support provided by CONACYT-México (Grant PN6281_2017) and Fondo CONACYT-SENER-HIDROCARBUROS (Grant FSCSH-2016-248090). H.E. Zilli-Tomita acknowledges the economic support provided by CIATEC. V.A. Suárez-Toriello, thank the Cátedras-CONACYT program (Project 965). The authors appreciate the help of Dra. Claudia Badillo and the facilities for access to the DRX instrument (Grant INFRA20115-253602 from CONACYT-México). We appreciate the assistance of Dr. René Rangel and Dra. Elizabeth Diane-Issacs and LANBAMA for the nitrogen adsorption measurements. The laboratory assistance of Ing. Catalina de la Rosa Juárez is also appreciated.

Declarations

Conflict of interest All the authors declare no conflict of interest.

References

1. Predel, H.: Petroleum Coke, Ullmann's encyclopedia of industrial chemistry (2006)
2. Caruso, J.A., Zhang, K., Schroeck, N.J., McCoy, B., McElmurry, S.P.: Petroleum coke in the urban environment: a review of potential health effects. Int J Env Res Pub He **12**(6), 6218–6231 (2015)
3. Shan, Y., Guan, D., Meng, J., Liu, Z., Schroeder, H., Liu, J., Mi, Z.: Rapid growth of petroleum coke consumption and its related emissions in China. Appl. Energy **226**, 494–502 (2018)
4. Administration USEI (2016) Carbon dioxide emission coefficients. https://www.eia.gov/environment/emissions/co2_vol_mass.php. Accessed 6 Feb 2020
5. Puig-Gamero, M., Lara-Díaz, J., Valverde, J.L., Sanchez-Silva, L., Sánchez, P.: Dolomite effect on steam co-gasification of olive pomace, coal and petcoke: TGA-MS analysis, reactivity and synergistic effect. Fuel **234**, 142–150 (2018)
6. Olmeda, J., Sánchez de Rojas, M.I., Frías, M., Donatello, S., Cheeseman, C.R.: Effect of petroleum (pet) coke addition on the density and thermal conductivity of cement pastes and mortars. Fuel **107**, 138–146 (2013)
7. Nemanova, V., Abedini, A., Liliedahl, T., Engvall, K.: Co-gasification of petroleum coke and biomass. Fuel **117**, 870–875 (2014)
8. Yuzbasi, N.S., Selçuk, N.: Air and oxy-fuel combustion behavior of petcoke/lignite blends. Fuel **92**(1), 137–144 (2012)
9. Menéndez, J.A., Pis, J.J., Alvarez, R., Barriocanal, C., Fuente, E., Díez, M.A.: Characterization of petroleum coke as an additive in metallurgical cokemaking. Modification of thermoplastic properties of coal. Energ. Fuel. **10**(6), 1262–1268 (1996)
10. Briceño, S., Brämer-Escamilla, W., Silva, P., García, J., Del Castillo, H., Villarroel, M., Rodriguez, J.P., Ramos, M.A., Morales, R., Diaz, Y.: NiFe2O4/activated carbon nanocomposite as magnetic material from petcoke. J. Magn. Magn. Mater. **360**, 67–72 (2014)
11. Tan, K.B., Vakili, M., Horri, B.A., Poh, P.E., Abdullah, A.Z., Salamatinia, B.: Adsorption of dyes by nanomaterials: recent developments and adsorption mechanisms. Sep. Purif. Technol. **150**, 229–242 (2015)
12. Chakrabarti, S., Dutta, B.K.: Photocatalytic degradation of model textile dyes in wastewater using ZnO as semiconductor catalyst. J. Hazard. Mater. **112**(3), 269–278 (2004)
13. Ren, H.-T., Yang, Q.: Fabrication of Ag2O/TiO2 with enhanced photocatalytic performances for dye pollutants degradation by a pH-induced method. Appl. Surf. Sci. **396**, 530–538 (2017)
14. Zangeneh, H., Zinatizadeh, A.A.L., Habibi, M., Akia, M., Hasnain Isa, M.: Photocatalytic oxidation of organic dyes and pollutants in wastewater using different modified titanium dioxides: a comparative review. J. Ind. Eng. Chem. **26**, 1–36 (2015)
15. Moezzi, A., McDonagh, A.M., Cortie, M.B.: Zinc oxide particles: synthesis, properties and applications. Chem. Eng. J. 185–186 1–22 (2012)
16. Pant, B., Park, M., Kim, H.-Y., Park, S.-J.: Ag-ZnO photocatalyst anchored on carbon nanofibers: synthesis, characterization, and photocatalytic activities. Synth. Met. **220**, 533–537 (2016)
17. Pant, B., Ojha, G.P., Kim, H.-Y., Park, M., Park, S.-J.: Fly-ash-incorporated electrospun zinc oxide nanofibers: potential material for environmental remediation. Environ. Pollut. **245**, 163–172 (2019)
18. Lee, K.M., Lai, C.W., Ngai, K.S., Juan, J.C.: Recent developments of zinc oxide based photocatalyst in water treatment technology: a review. Water Res. **88**, 428–448 (2016)
19. Maučec, D., Šuligoj, A., Ristić, A., Dražić, G., Pintar, A., Tušar, N.N.: Titania versus zinc oxide nanoparticles on mesoporous silica supports as photocatalysts for removal of dyes from wastewater at neutral pH. Catal. Today **310**, 32–41 (2018)
20. Matos, J., Arcibar-Orozco, J., Poon, P.S., Pecchi, G., Rangel-Mendez, J.R.: Influence of phosphorous upon the formation of DMPO-OH and POBN-$O2^{-}$ spin-trapping adducts in carbon-supported P-promoted Fe-based photocatalysts. J Photoch Photobio A **391**, 112362 (2020)
21. Pant, B., Pant, H.R., Barakat, N.A.M., Park, M., Jeon, K., Choi, Y., Kim, H.-Y.: Carbon nanofibers decorated with binary semiconductor (TiO2/ZnO) nanocomposites for the effective removal of organic pollutants and the enhancement of antibacterial activities. Ceram. Int. **39**(6), 7029–7035 (2013)
22. Matos, J., Laine, J., Herrmann, J.-M.: Effect of the type of activated carbons on the photocatalytic degradation of aqueous organic pollutants by UV-irradiated titania. J. Catal. **200**(1), 10–20 (2001)
23. Giannakoudakis, D.A., Arcibar-Orozco, J.A., Bandosz, T.J.: Effect of GO phase in Zn(OH)2/GO composite on the extent of photocatalytic reactive adsorption of mustard gas surrogate. Appl. Catal. B-Environ. **183**, 37–46 (2016)
24. Bandosz, T.J., Jagiello, J., Contescu, C., Schwarz, J.A.: Characterization of the surfaces of activated carbons in terms of their acidity constant distributions. Carbon **31**(7), 1193–1202 (1993)
25. Thommes, M., Kaneko, K., Neimark, A.V., Olivier, J.P., Rodriguez-Reinoso, F., Rouquerol, J., Sing, K.S.W.: Physisorption of gases, with special reference to the evaluation of surface area and pore size distribution (IUPAC Technical Report). Pure Appl. Chem. **87**(9–10), 1051–1069 (2015)
26. Lowell, S.S., Joan, E., Martin. A.T., Matthias, T.: Characterization of porous solids and powders: surface area, pore size and density. particle technology series. Kluwer Academic, The Netherlands, 346 (2004)
27. Mott, N.F., Davis, E.A.: Electronic processes in non-crystalline materials. OUP Oxford (2012)
28. Kumar, V., Kumari, S., Kumar, P., Kar, M., Kumar, L.: Structural analysis by Rietveld method and its correlation with optical properties of nanocrystalline zinc oxide. Adv. Mater. Lett **6**(2), 139–147 (2015)
29. Chen, J.-L., Devi, N., Li, N., Fu, D.-J., Ke, X.-W.: Synthesis of Pr-doped ZnO nanoparticles: their structural, optical, and photocatalytic properties. Chin. Phys. B **27**(8), 086102 (2018)
30. Ramimoghadam, D., Hussein, M.Z., Taufiq-Yap, Y.H.: The effect of sodium dodecyl sulfate (SDS) and cetyltrimethylammonium bromide (CTAB) on the Properties of ZnO synthesized by hydrothermal method. Int. J. Mol. Sci. **13**(10), 13275–13293 (2012)
31. Arcibar-Orozco, J.A., Giannakoudakis, D.A., Bandosz, T.J.: Copper hydroxyl nitrate/graphite oxide composite as superoxidant for the decomposition/mineralization of organophosphate-based chemical warfare agent surrogate. Adv. Mater. Interfaces **2**(16) (2015)
32. Wu, Q.-y, Liang, H.-q, Li, M., Liu, B.-t, Xu, Z.-k: Hierarchically porous carbon membranes derived from PAN and their selective adsorption of organic dyes. Chin. J. Polym. Sci. **34**(1), 23–33 (2016)
33. Kumar, M., Tamilarasan, R.: Modeling of experimental data for the adsorption of methyl orange from aqueous solution using a low cost activated carbon prepared from Prosopis juliflora. Pol. J. Chem. Technol. **15**(2), 29–39 (2013)
34. Chen, X., Wu, Z., Gao, Z., Ye, B.C.: Effect of different activated carbon as carrier on the photocatalytic activity of Ag-N-ZnO photocatalyst for methyl orange degradation under visible light irradiation. Nanomaterials (Basel) **7**(9) (2017)
35. Posa, V.R., Annavaram, V., Koduru, J.R., Ammireddy, V.R., Somala, A.R.: Graphene-ZnO nanocomposite for highly efficient photocatalytic degradation of methyl orange dye under solar light irradiation. Korean J. Chem. Eng. **33**(2), 456–464 (2016)

36. Farag, H.K., Aboelenin, R.M., Fathy, N.A.: Photodegradation of methyl orange dye by ZnO loaded onto carbon xerogels composites. Asia-Pac. J. Chem. Eng. **12**(1), 4–12 (2017)
37. Wu, H., Lin, S., Chen, C., Liang, W., Liu, X., Yang, H.: A new ZnO/rGO/polyaniline ternary nanocomposite as photocatalyst with improved photocatalytic activity. Mater. Res. Bull. **83**, 434–441 (2016)
38. Jamil, T.S., Ghaly, M.Y., Fathy, N.A., Abd el-halim, T.A., Österlund, L.: Enhancement of TiO2 behavior on photocatalytic oxidation of MO dye using TiO2/AC under visible irradiation and sunlight radiation. Sep. Purif. Technol. **98**, 270–279 (2012)
39. Borade, P.A., Suroshe, J.S., Bogale, K., Garje, S.S., Jejurikar, S.M.: Photocatalytic performance of ZnO carbon composites for the degradation of methyl orange dye. Mater. Res. Express **7**(1), 015512 (2020)
40. Gamarra Guere, C., La Rosa-Toro, G.A.: Discoloration of methyl orange by fenton process. Rev Soc Quím Perú. **80**(1), 24–34 (2014)